

Flexural behavior of corroded HPS beams

Jianxin Peng^a, Linfa Xiao^{a,*}, Jianren Zhang^a, C.S. Cai^b, Lei Wang^a

^a School of Civil Engineering, Changsha University of Science and Technology, Changsha, Hunan 410114, China

^b Department of Civil and Environmental Engineering, Louisiana State University, Baton Rouge, LA 70803, USA

ARTICLE INFO

Keywords:

High performance steel (HPS)
Flexural behavior
3D scanning technology
Random corrosion
Analytical model

ABSTRACT

Experimental research is conducted to investigate the flexural behavior of corroded High Performance Steel (HPS) beams. Four beams with various corrosion damage are designed and subjected to electrochemical accelerated corrosion process. 3D scanning technology is employed to analyze the geometric features affected by the corrosion damage. Flexural tests are carried out, and the impact of corrosion on the flexural response is discussed. Considering the randomness of corrosion pits in each area, predictive models are proposed for the flexural strength of corroded beams with an idealized elastic-plastic and linear-hardening constitutive relationship model. An analysis comparing the proposed models with Chinese and American codes is made. Results show that increasing the corrosion damage leads to a decrease of discreteness in the residual sectional area and causes a transformation in the compressed flange from noncompact to slender. A corrosion loss less than 10% leads to slight deterioration of both strength and stiffness degradation, while further corrosion damage results in a significant decrease. The depth and length of the buckling wavelength for corroded beams decreases gradually as the corrosion damage become more serious. The analytical models IEM and LHM or the GB50017-2017 may be suitable for predicting the lower and upper limit values of the ultimate flexural moment, respectively, and results predicted by AISC are conservative.

1. Introduction

High performance steel (HPS) is considered to have higher strength, better ductility, and a lower thickness effect than ordinary steel and many significant applications have been carried out because of the exceptional properties of HPS, such as the Minato Ohashi Bridge [1], the Millau Bridge [2], and National Stadium (Bird's Nest) [3]. Extensive research has been conducted to investigate the mechanical properties of HPS on the basis of material tests [4,5]. Some efforts [6–8] on flexural ductility and buckling behavior have also been carried out. Felkel et al. [9] conducted monotonic and cyclic tests and computer simulations of HPS 70W girders. Barth et al. [10] evaluated the application of a simplified moment redistribution to hybrid HPS 485W bridge girders in negative flexural region. The above studies of the intact specimen are significant for the HPS application of new structures. Additionally, HPS has various definitions in different countries according to the excellent properties adopted, and this paper focuses on high strength steel.

Corrosion is a common deterioration cause in engineering structures, especially for steel members exposed to a wet and salt spray environment [11,12]. For example, it is reported that 15% of the highway steel bridges replacements and some 50% of the railway bridges replacements in Japan were caused by corrosion [13]. This is an

unavoidable phenomenon due to the spalling of coating affected by the environment, load, chemical reactions, and other factors [14]. In all forms of corrosion, general corrosion is regarded as a prevalent situation [15]. It is often caused by the accumulation of water and salt, especially for the steel located at marine environment or the deicing zone. It may cause a reduction of bearing capacity and ductility as the mechanical properties and sectional characteristics have been changed [16,17]. The consequences of this deterioration generally range from the progressive weakening of a structure over a long period of time to sudden structural failure [18,19].

Some investigations have been made into the degradation mechanism of structural performance for HPS structures damaged from corrosion. Wu et al [20] investigated the corrosion behavior and mechanism of E690 high-strength steel under different pH values using electrochemical technology and long-term alternating wet-dry cycle experiments and established a relationship between pH values and the corrosion mechanism. Ma et al [21] analyzed the impact of cathodic potential on the stress corrosion cracking of E690 steel in simulated seawater. López et al [22] studied the tribocorrosion behavior of High-Strength Low-Alloy Steel and the material degradation mechanism. Akiyama et al [23] evaluated the hydrogen embrittlement of corroded high-strength steels and obtained a power law relationship between the

* Corresponding author.

E-mail address: linfa_x@163.com (L. Xiao).

<https://doi.org/10.1016/j.engstruct.2019.06.006>

Received 11 December 2018; Received in revised form 6 May 2019; Accepted 4 June 2019

Available online 10 June 2019

0141-0296/ © 2019 Elsevier Ltd. All rights reserved.

notch tensile strength of hydrogen precharged specimens and diffusible hydrogen content. However, very few studies have been reported regarding the degradation of the flexural behavior of corroded HPS structures, especially considering the randomness of corrosion. The existing Chinese design specifications [24] apply to intact steel with a yield strength less than 460 MPa. Additionally, existing design methods are based on the results of ordinary steels. The impact of corrosion on strengths and failure modes of HPS structures has not been sufficiently researched, and its evaluation method has not been clearly established. This may result in unpredictable consequences in regards to the assessment of safety and service life of structures.

To capture the true randomness of corrosion pits, 3D optical measurement is employed as a powerful tool in this paper. Compared with the traditional method which is regarded as a repeated, time-consuming and inaccurate measurement, 3D optical measurement can automatically reconstruct the shape of specimens and conveniently obtain geometric dimensions without considering the influence of complex surfaces [25,26]. Wang et al [27] developed virtual models to analyze the residual area of corroded bars using 3D scanning technology. Mancini et al [28] evaluated the local damage of reinforcing bars based on 3D scanning data and found that both corrosion and cyclic loading led to a more evident concentration of corrosion. Tang et al [29] conducted a series of statistical analyses using a 3D laser scanner and found that corrosion changes the fracture mode of deformed steel bars. This research proves the feasibility of using 3D scanning technology on corroded structures.

The objective of this study is to investigate the flexural behavior of random corroded HPS beams through a series of flexural tests. Four HPS beams were designed, and three of them were subjected to an electrochemical accelerated corrosion process. The geometric features of the specimens were quantified using 3D scanning technology. The flexural behavior of the tested beams affected by corrosion was discussed. Further, iterative models considering two constitutive relationships were proposed to analyze the flexural properties, and a comparison between the experimental results, proposed model, AISC 360-10 [30], and GB50017-2017 were made. Several conclusions of findings were then drawn according to the proposed study.

2. Experimental program

In this section, details of the specimens are first described. The accelerated corrosion tests are carried out to obtain the designed corrosion levels. Then, tensile tests are accomplished to determine the material properties of the corroded specimens. Subsequently, loading tests are performed to evaluate the flexural behavior of the corroded HPS beams. Details are presented as follows.

2.1. Details of specimens

A total of 4 welded HPS beams were fabricated in the experimental program, including one reference specimen and three corroded specimens as shown in Table 1. The specimens with designed corrosion levels ρ_d of 0%, 5%, 10%, and 15% were numbered CB0, CB5, CB10, and CB15, respectively. As shown in Fig. 1, the intact beam had a length of 2000 mm and a height of 200 mm, a flange with a 150 mm width and an 8 mm thickness, and a web with a 184 mm height and an 8 mm

Table 1
Summary of HPS Specimens.

No.	Designed corrosion level ρ_d	Quantity
CB0	0	1
CB5	5%	1
CB10	10%	1
CB15	15%	1

thickness. Transverse stiffeners with 6 mm thickness and 71 mm width were placed at the loading points, reaction points, and 350 mm away from supports.

2.2. Accelerated corrosion test and scanning

Electrochemically accelerated corrosion tests were performed to obtain the designed corrosion levels for the corroded specimens. The specimens were immersed in a sink with a 5% sodium chloride solution, as shown in Fig. 2. Stainless steel plates were placed vertically in the sink and parallel to the flange. The beams linked to the positive output served as the anode, and the stainless steel plate linked to the negative output served as the cathode. The imposed corrosion current was 1880 mA during the accelerated corrosion process. The duration of the applied corrosion current was estimated by Faraday's law [31], which can be expressed as follows:

$$t = 2\rho_d eNm_0/mI \quad (1)$$

where e = the electron charge; N = the Avogadro constant; m_0 = the initial mass of beam; m = the mass of beam after corrosion; and I = the corrosion current.

The geometrical features of these specimens were determined using 3D scanning technology following the corrosion test. Geometric models of the corroded specimens were rebuilt using a 3D scanning device (see Fig. 3) with a 29 μ m accuracy. Optimized operations of the point cloud data after scanning, such as filtering and noise processing, were carried out. Models for the curved surfaces were developed using the Geomagic software after wrapping, repairing, and grid division. The geometrical features, including thickness and section area, were measured.

2.3. Material properties

The material properties of corroded HPS specimens were analyzed using tensile tests in previous research [32]. It was found that corrosion changes the fracture morphology of specimens from crescent to irregular shape and the maximum cross-sectional loss ratio is reasonable to evaluate the mechanical behavior of the corroded steel specimens. The relationships between yield and ultimate strength and corrosion level were established as described in Eq. (2). The ductility and failure mechanism of the corroded specimens was discussed, and a simplified three-stage constitutive model of HPS specimens was proposed as shown in Eq. (3).

$$f_{iry} = -314.46\eta_s^2 - 282.11\eta_s + 567.72$$

$$f_{iru} = -301.6\eta_s^2 + 317.61\eta_s + 688.22 \quad (2)$$

where η_s = the maximum cross-sectional loss ratio; f_{iry} = the yield strength; and f_{iru} = the ultimate strength.

$$\sigma_n = \begin{cases} E_s \varepsilon_n, & 0 \leq \varepsilon_n \leq \varepsilon_{ny} \\ f_{ny}, & \varepsilon_{ny} < \varepsilon_n \leq \varepsilon_h \\ f_{ny} + (f_{nu} - f_{ny})(\varepsilon_n - \varepsilon_h)/(\varepsilon_u - \varepsilon_h), & \varepsilon_h < \varepsilon_n \leq \varepsilon_u \end{cases} \quad (3)$$

where E_s = the modulus elasticity of corroded specimens; f_{ny} and f_{nu} = the nominal yield strength and the nominal ultimate strength, respectively; ε_{ny} , ε_h , and ε_u = the nominal yield strain, the hardening strain, and the ultimate strain, respectively; and σ_n and ε_n = the nominal stress and nominal strain, respectively.

2.4. Flexural test arrangement

Fig. 4 shows the loading schemes, lateral bracing and measuring point layout. The specimens were tested using a four-point flexural test with a 1000 kN capacity actuator. Two pairs of lateral braces were arranged at the loading points to prevent lateral deformation [33,34]. The tested beams were simply supported, and the lateral deflection and

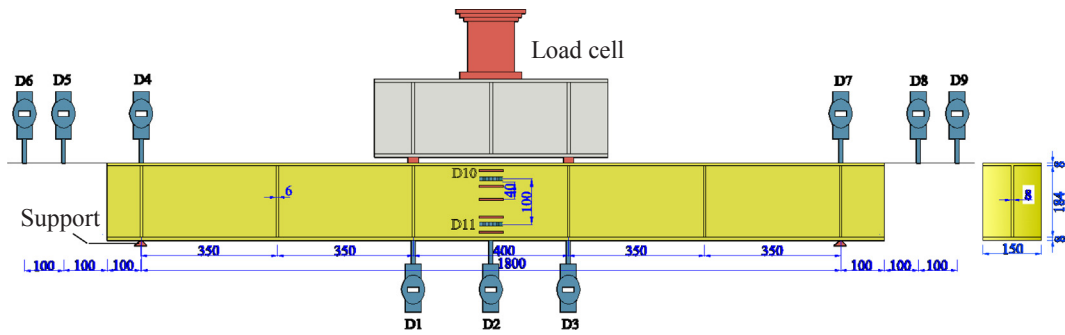


Fig. 1. Detailed dimensions of the intact beam (mm).

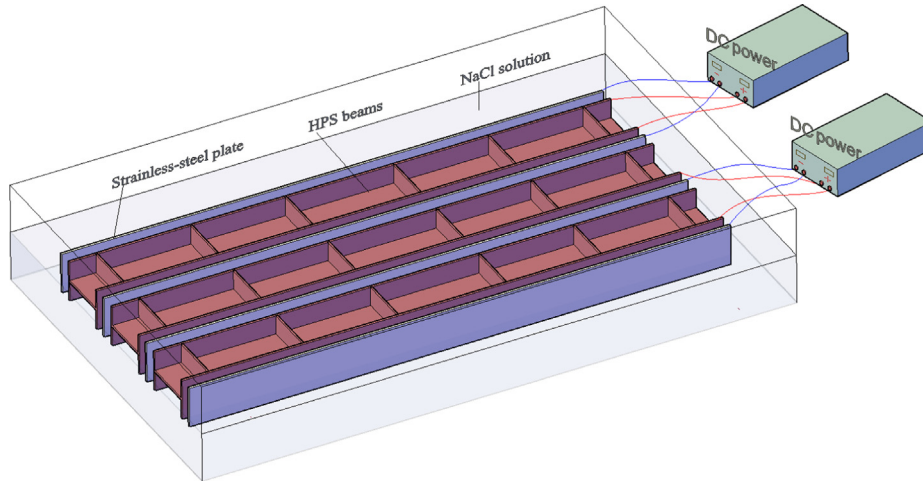


Fig. 2. Schematic diagram of accelerated corrosion test.



Fig. 3. 3D scanning device.



Fig. 4. Loading device diagram.

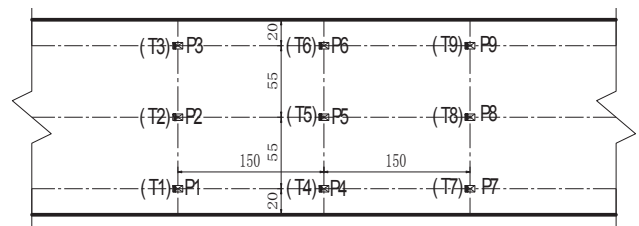


Fig. 5. Positions of strain measuring points.

twist rotation were restricted by clamped plates. The vertical displacement at the support, loading points, and mid-span were recorded by five dial gauges, as shown in Fig. 1. The rotations of the tested beams were measured by two dial gauges that are located at both ends of the beam. Two dial gauges 100 mm apart were attached to the web. Thus the lateral rotation of each beam can be calculated using a method in which the difference of the vertical displacement is divided by the horizontal distance of the two dial gauges. The strains of the web at the

mid-span section were measured using five strain gauges, and the strains of both the top flange and the bottom flange were recorded using three strain gauges at the middle of the flange and six strain gauges at a distance of 150 mm away from the middle section, as shown in Fig. 5.

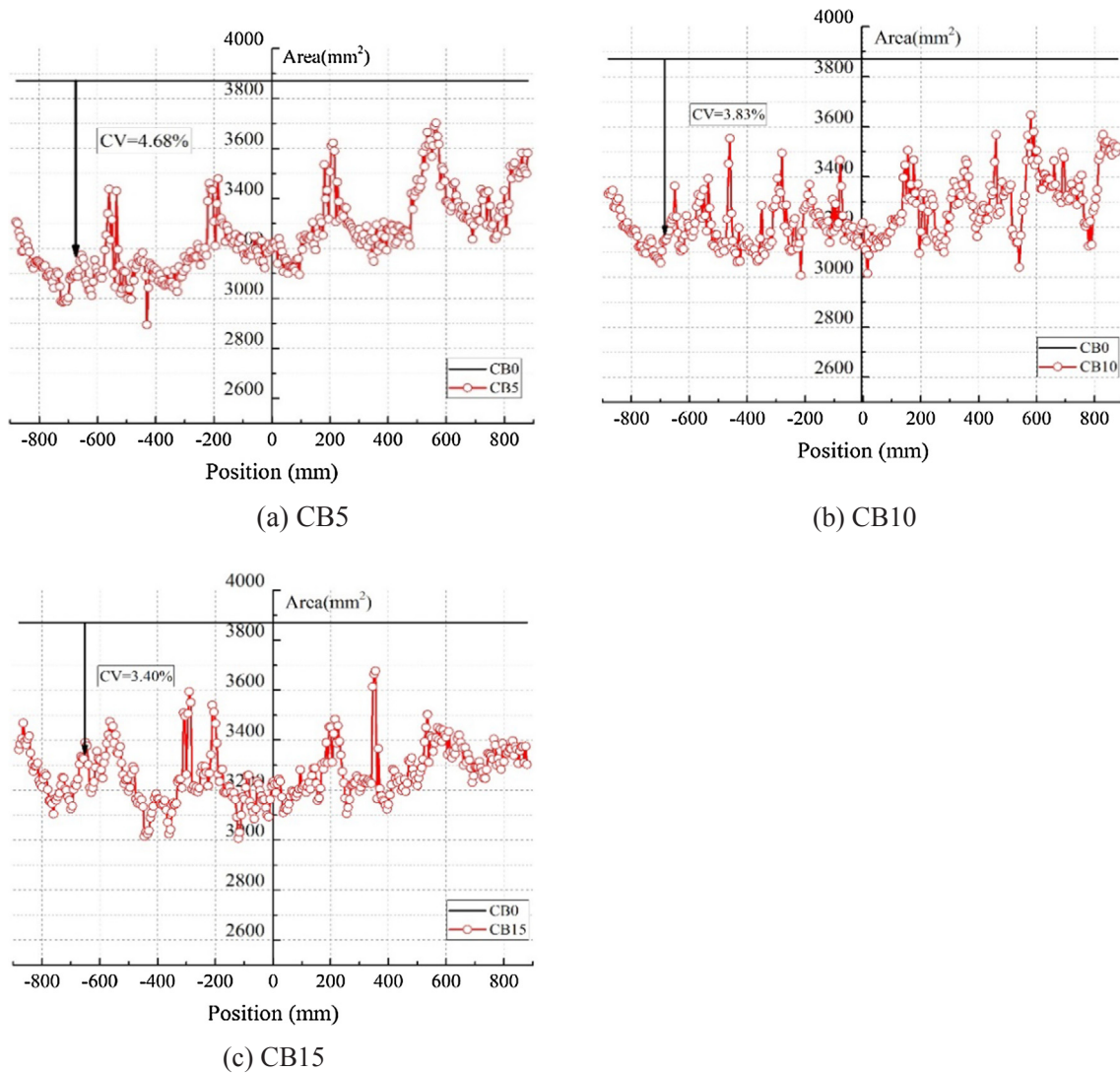


Fig. 6. Longitudinal distribution of the cross-sectional area.

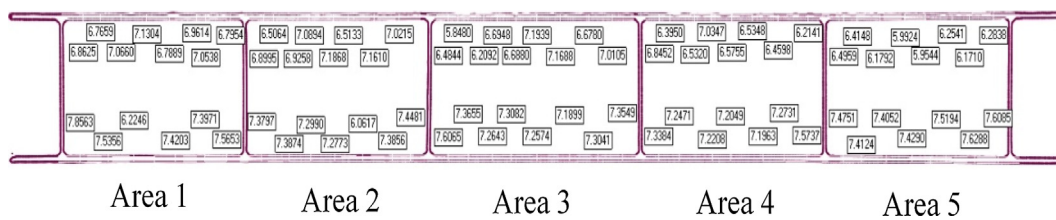


Fig. 7. Dimensional measurement.

The test procedure for the tested beams consisted of four steps: (1) repeated preloading and unloading until the instruments were in perfect contact; (2) loading with an increment of 20 kN during elastic loading region; (3) loading with an increment of 10 kN after attaining yield strain until the maximum capacity; and (4) unloading slowly to obtain sufficient deformation information. During the test, the applied load and resulting strains were obtained using a load cell and a data acquisition system, and the displacements were recorded manually.

3. Test results and discussion

3.1. Geometric characteristics

Residual sectional areas with a spacing of 5 mm along the specimens

were obtained with the Geomagic software. As shown in Fig. 6, the Discrete Coefficient (CV), which is defined as the mean value of its cross-sectional area divided by its standard deviation, expresses the discreteness of the residual sectional area of corroded beams. The cross-sectional area varies in all locations, and there is no regularity, which reflects the heterogeneity of corrosion. As the degree of corrosion increases, the CV value diminishes from 4.68% to 3.40%. This is because at the initial stage of corrosion, the local corrosion dominates and the cross-sectional area fluctuates greatly. When beams are subjected to serious levels of corrosion, the range of stripping caused by corrosion is larger, and then the sectional area tends to be stable.

Additionally, a large number of random measurements were performed to determine the detailed size of each component. As shown in Fig. 7, dimensions of the components in each area are different. The size

Table 2
Thickness of Components.

Position	Component	CB0		CB5		CB10		CB15	
		T(mm)	ρ_A (%)						
Area 1	Compressed flange	8	0	7.60	5.0%	7.18	10.2%	6.42	19.7%
	Web	8	0	7.37	7.9%	6.88	14.1%	6.51	18.6%
	Tensioned flange	8	0	6.90	13.8%	6.68	16.5%	5.92	26.0%
Area 2	Compressed flange	8	0	6.86	14.3%	6.80	15.0%	6.71	16.2%
	Web	8	0	7.85	1.8%	7.20	10.0%	6.23	22.1%
	Tensioned flange	8	0	6.96	13.0%	6.59	17.6%	5.89	26.4%
Area 3	Compressed flange	8	0	7.64	4.6%	6.98	12.7%	6.61	17.3%
	Web	8	0	7.38	7.8%	6.87	14.1%	6.50	18.8%
	Tensioned flange	8	0	6.57	17.9%	6.43	19.6%	6.20	22.6%
Area 4	Compressed flange	8	0	6.86	14.2%	6.69	16.3%	7.12	11.0%
	Web	8	0	7.56	5.5%	7.07	11.6%	6.70	16.3%
	Tensioned flange	8	0	7.28	9.0%	5.67	29.2%	4.89	38.9%
Area 5	Compressed flange	8	0	7.10	11.2%	6.80	15.0%	6.51	18.7%
	Web	8	0	7.67	4.1%	7.34	8.3%	6.96	13.0%
	Tensioned flange	8	0	7.54	5.8%	6.27	21.6%	5.80	27.5%
Average	Compressed flange	8	0	7.21	9.9%	6.89	13.9%	6.67	16.6%
	Web	8	0	7.57	5.4%	7.07	11.6%	6.58	17.8%
	Tensioned flange	8	0	7.05	11.9%	6.33	20.9%	5.74	28.3%

Table 3
Slenderness of components.

No.	λ_{fc}			λ_{fw}		λ_{ft}		
	Experiment	Upper limit λ_u	Lower limit λ_l	Experiment	Lower limit λ_l	Experiment	Upper limit λ_u	Lower limit λ_l
CB0	9.38	9.83	6.67	23.00	65.97	9.38	9.83	6.67
CB5	10.40	10.17	6.90	24.31	68.92	10.64	10.27	6.97
CB10	10.89	10.16	6.90	26.03	67.02	11.85	10.37	7.04
CB15	11.24	10.26	6.96	27.96	67.91	13.07	10.44	7.09

Note: ρ_A = the average corrosion level of each component; and λ_{fc} , λ_{ft} and λ_{fw} = slenderness of compressed flange, tensioned flange and web, respectively.

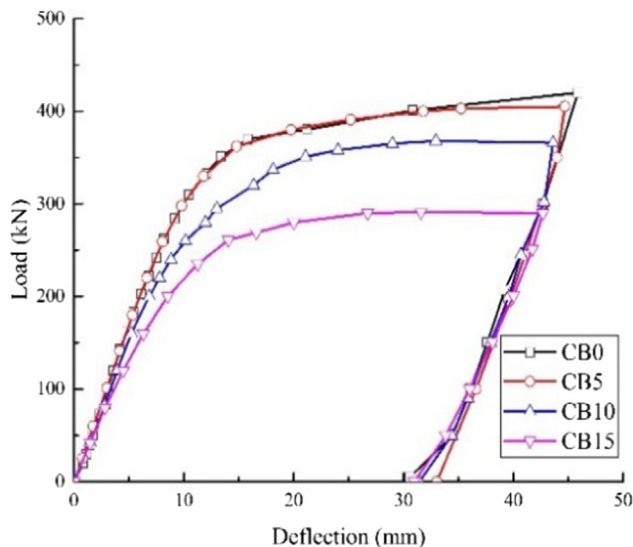


Fig. 8. Load-vertical deflection curves.

of the compressed flange, tensioned flange and web in the same area are relatively uniform. The thickness and corrosion level at the top and bottom flange and web are listed in Table 2. According to Eqs. (4)–(7), which is supported by AASHTO LRFD [35], the slenderness of the flanges λ_f and the web λ_w is calculated based on the average thickness and listed in Table 3. The tensioned flange has the most serious corrosion level that varies from 11.9% to 28.3%, which leads to λ_{ft}

changing from 9.38 to 13.07. The compressed flange shows less corrosion damage, which does not exceed 16.6%. The λ_{fc} ranges from 9.38 to 11.24, which exceeds the upper limit λ_u for corroded tested beams. As a result, the compressed flange transforms from noncompact to slender. The corrosion level of the web is close to the design value, and the λ_w is less than the lower limit λ_l . This means that the web belongs to a compact section. These changes of sectional characteristics may affect the flexural behavior of the corroded steel beams. It is noted that the local buckling of the compression flange may occur before the global failure. In order to avoid premature local buckling failure, the flange with higher corrosion degree is selected as the tension flange.

For compact section

$$\lambda_f = b_f/2t_f \leq 0.38\sqrt{E/f_{yc}} \tag{4}$$

$$\lambda_w = h_w/t_w \leq 3.76\sqrt{E/f_{yw}} \tag{5}$$

For non-compact section

$$0.38\sqrt{E/f_{yc}} \leq \lambda_f = b_f/2t_f \leq 0.56\sqrt{E/f_{yc}} \tag{6}$$

$$3.76\sqrt{E/f_{yw}} \leq \lambda_w = h_w/t_w \leq 5.7\sqrt{E/f_{yw}} \tag{7}$$

where b_f = the width of flange; t_f and t_w = the thickness of flange and web, respectively; f_{yc} and f_{yw} = the yield strength of flange and web, respectively; and h_w = the height of web.

3.2. Load-deflection response

Fig. 8 shows the results obtained from the tests in terms of load–deflection curves of the mid-span. The curves keep linear at the initial

loading stage, without stiffness degradation. When they enter the elastic-plastic stage, the curves show a nonlinear growth, and the deflection increases faster than the applied load. The stiffness of the specimens drops sharply when approaching the ultimate load. During unloading, the curves are roughly parallel to the curves at the initial stage, which means that the stiffness of these two stages is similar.

These curves are quite different due to the varying degrees of corrosion damage, which are manifested on the degradation of stiffness and strength. For example, the slightly corroded beam CB5 has a similar stiffness as that of CB0 at the initial stage, while the stiffness of the severely corroded beam CB15 is significantly lower than that of the reference beam. The ultimate load of CB5 has a 4% decrease as compared to CB0. The degradation of the ultimate load for CB10 and CB15 is 3.3 and 7.8 times that of CB5, respectively. Therefore, it can be considered that slight corrosion loss, within 10%, has little impact on strength and stiffness degradation, and severe corrosion results in a significant reduction of both strength and stiffness. While the number of specimens studied is limited, the influence of corrosion on HPS is till confirmed.

3.3. Load-strain behavior

Strain results of the web are plotted in Fig. 9 for all of the tested beams. It can be observed that the strains vary approximately linearly across the height before the ultimate load. With an increase of the corrosion level, the tensile strains appear slightly nonlinear when approaching the ultimate load as result of the action of both complex stresses and severe corrosion damage. In general, severe corrosion also causes the neutral axis to move toward the compressive zone, though each specimen is different. This is mainly due to the more serious corrosion level of the tensile flange than the compressive flange.

Fig. 10 shows the load-strain relationship of the flanges at the mid-span section for CB0 and CB15. Initially, the strain grows linearly, and the magnitudes of the strains for the compressed flange and tensioned flange are close. This indicates that only in-plane flexural behavior develops during this stage. At a certain load of 200 kN for CB0, strains develops nonlinearly. Also, the difference of the strain readings of the compressed flange begins to increase, which is caused by the lateral torsion deformation rather than the local buckling [36,37], and the strain value at this time has not reached the yield strain. When the applied load is close to the ultimate load, strains P4, P5, and P6 of CB0

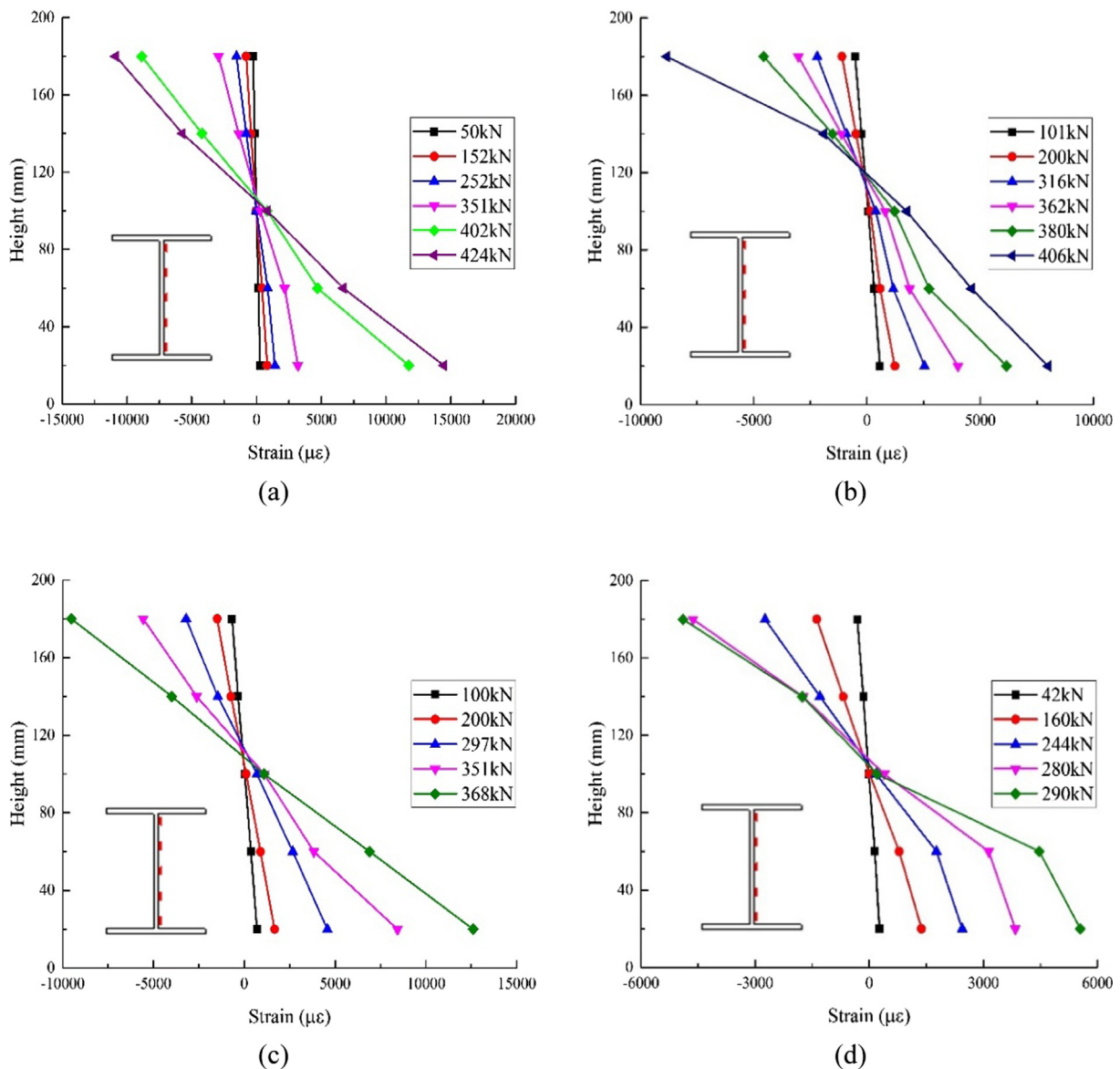


Fig. 9. Strains of the web along the height: (a) CB0; (b) CB5; (c) CB10; and (d) CB15.

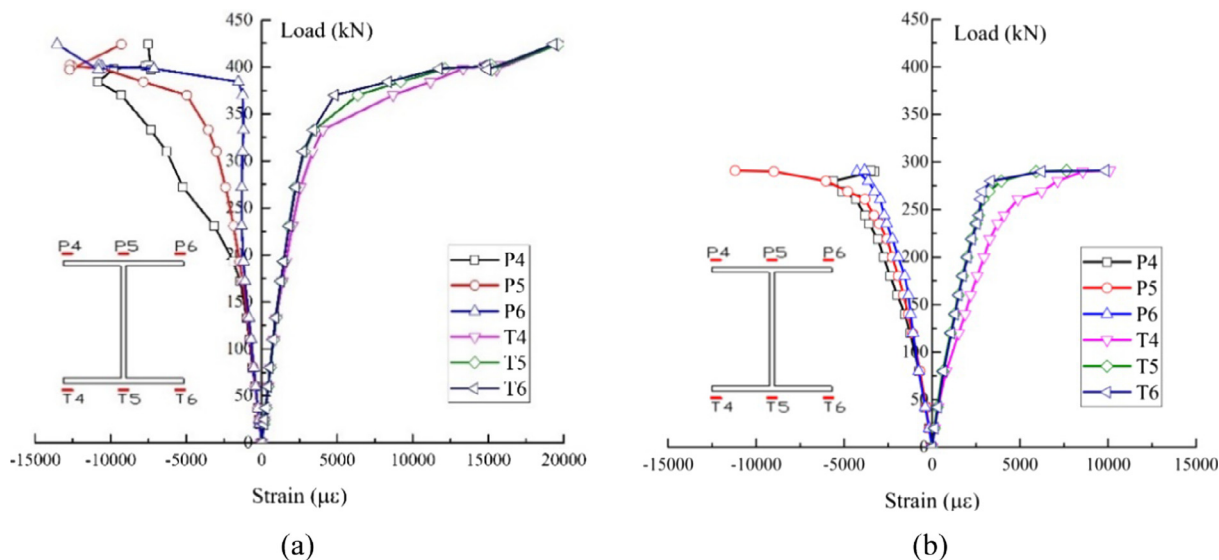


Fig. 10. Strains of flange: (a) CBO; and (b) CB15.

begins to decrease, which suggests the occurrence of local buckling [37,38]. The strains of the tensioned flange are almost consistent during the whole loading process. This means that no significant out-of-plane flexural behavior is developed for the tensioned flange. The lateral torsion deformation phenomenon and local buckling behavior for CB15 appear at 150 kN and 269 kN, respectively. This means that corrosion causes these phenomena to occur prematurely. It may be due to the increase of the slenderness ratio and the reduction of the torsion resistance of the flange resulting from the thin compressed flange caused by corrosion. In addition, the slopes of strain for CB15 are higher than that of CBO, which indicates that the deformation and stress of the corroded beam develops faster. This is mainly attributed to the reduction of the moment of inertia because of corrosion.

The strains at the cantilever part of the flange for the two tested beams are presented in Fig. 11. The strains of the tensioned flange for CBO are quite close, which implies that the stress of the tensioned flange at the pure flexural section is uniform. The strains of the compressed flange begin to decrease after 375 kN, at which moment the local buckling occurs. However, an obvious discrepancy of the strains of the compressed flange for CB15 is found after 150 kN. The strain P6 tends to decrease after 269 kN and eventually develops into tensile strain,

which suggests that there is a significant local buckling.

Failure behaviors of the pure flexural section are shown in Fig. 12. The entire beam exhibits a degree of plastic flexural deformation. Local buckling of the compressed flange is observed for all of the specimens. Stiffeners at the loading point are marked to measure the depth and length of the buckling wavelength. The most obvious buckling wavelength depth for specimens from CBO to CB15 varies from 15 mm to 5 mm, and the length of them ranges from 30 mm to 10 mm. The deeper and longer buckling wavelength of CBO implies that the reference beam has better ductility and torsion resistance. The depth and length for the corroded beam decrease gradually since the buckling resistance of the compressed flange decreases gradually when the corrosion damage becomes serious. Some small buckling wavelength is found for the damaged beams, the primary cause of which is the uneven cross section caused by non-uniform corrosion.

4. Prediction of flexural strength

4.1. Analytical model of flexural behavior

As mentioned previously, failure of corroded steel beams is a

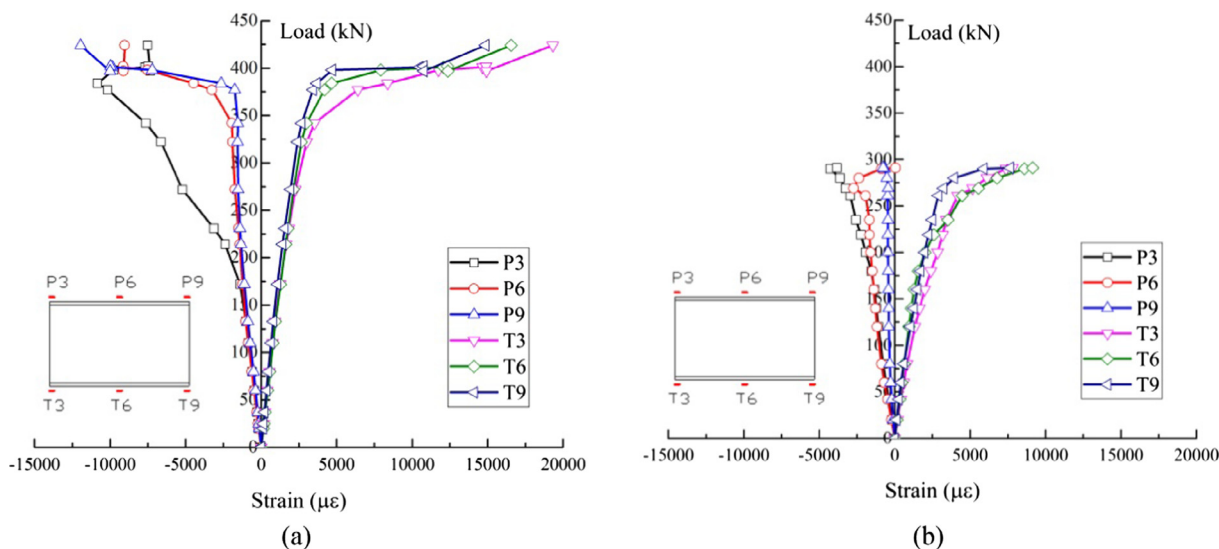


Fig. 11. Strains at the cantilever part of flange: (a) CBO; and (b) CB15.

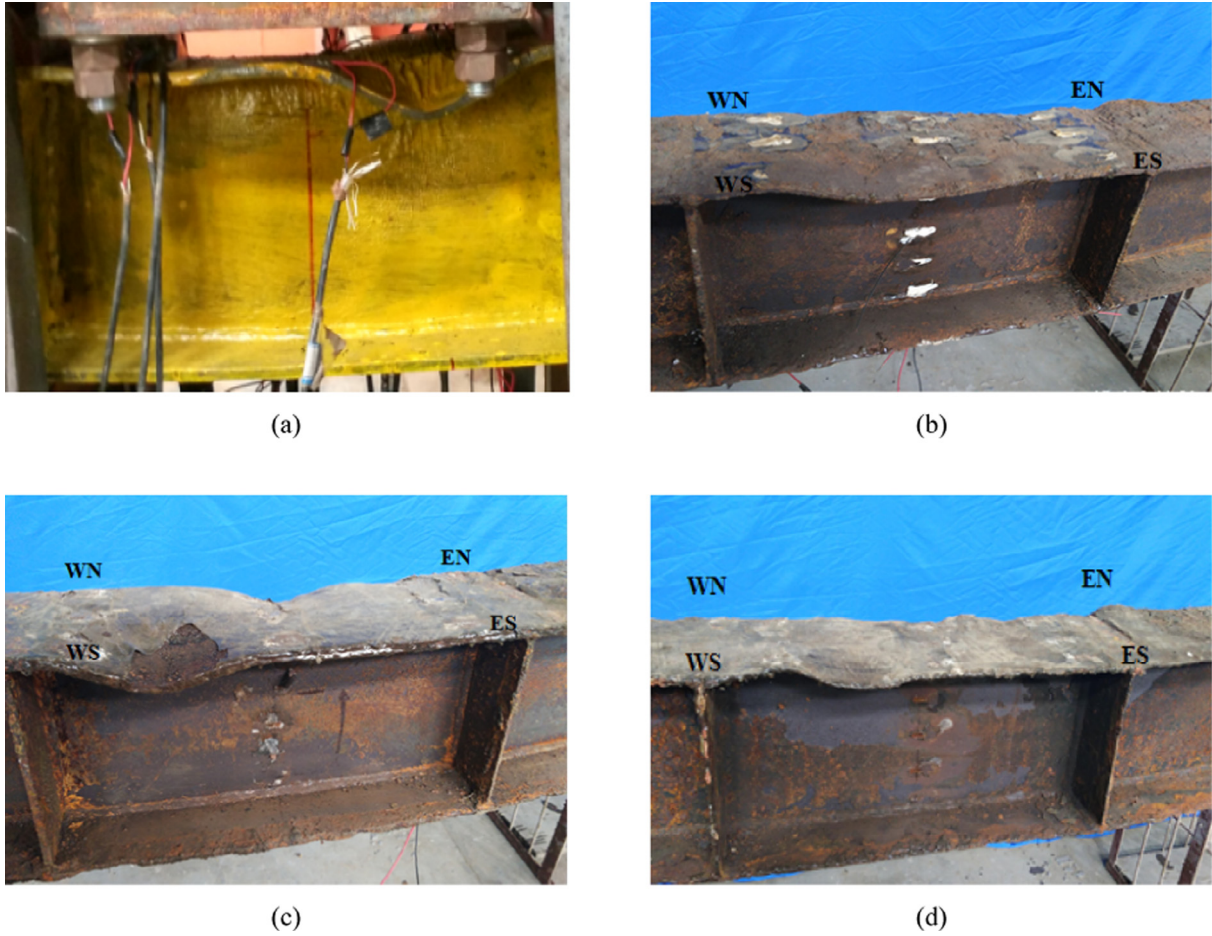


Fig. 12. Failure behaviors: (a) CB0; (b) CB5; (c) CB10; and (d) CB15.

complex behavior that includes local buckling, torsional buckling, etc. The existing codes may not be used to predict the strength of corroded HPS. In this study, a nonlinear iterative method is proposed to analyze the flexural behavior of corroded HPS beams. Then, the strength models for these specimens are proposed and compared with those from design specifications. While finite element method can always be used for this purpose, the proposed method provides a convenient alternative to establishing the flexural response model of the corroded HPS.

Simplistically, the three-stage constitutive model (Eq. (3)) is divided into two models, namely an idealized elastic-plastic model (IEM) and a linear-hardening model (LHM). The yielding platform of HPS is ignored since it is too short for HPS and will gradually disappear due to the effects of corrosion damage. The descent phase is not considered in the models since the purpose of this paper is to analyze the mechanical behavior of the beams before failure (as shown in Fig. 13). The expressions are shown as Eq. (8) for IEM and Eq. (9) for LHM, respectively.

$$\sigma_n = \begin{cases} E_s \varepsilon_n, & 0 \leq \varepsilon_n \leq \varepsilon_{ny} \\ f_{ny}, & \varepsilon_{ny} \leq \varepsilon_n \end{cases} \quad (8)$$

$$\sigma_n = \begin{cases} E_s \varepsilon_n, & 0 \leq \varepsilon_n \leq \varepsilon_{ny} \\ f_{ny} + E_{sp}(\varepsilon_n - \varepsilon_{ny}), & \varepsilon_{ny} \leq \varepsilon_n \end{cases} \quad (9)$$

where E_{sp} = the hardening modulus of corroded beams, and $E_{sp} = (f_{nu} - f_{ny}) / (\varepsilon_u - \varepsilon_n)$.

The stress reduction ratio of LHM due to strain hardening can be represented by $w(\varepsilon)$, and

$$w(\varepsilon) = \sigma_{AB} / \sigma_{AC} = (1 - E_{sp} / E_s)(1 - \varepsilon_{ny} / \varepsilon_n) \quad (10)$$

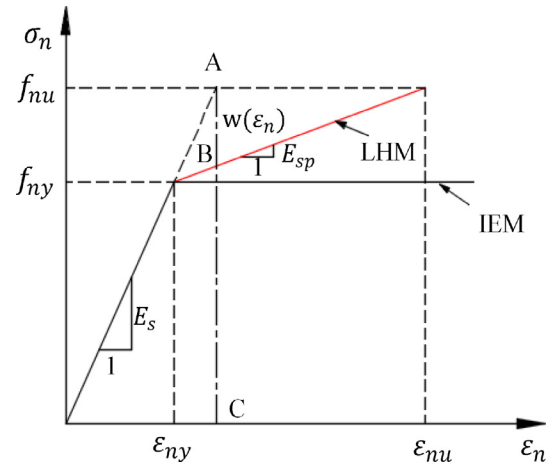


Fig. 13. Stress-strain relationship.

A real stress-strain relationship is used for the prediction of strength, which can be calculated by the following equations [39]

$$\begin{aligned} \sigma_{tr} &= \sigma_n(1 + \varepsilon_n) \\ \varepsilon_{tr} &= \ln(1 + \varepsilon_n) \end{aligned} \quad (11)$$

where σ_{tr} = the real stress; and ε_{tr} = the real strain.

Based on the corrosion characteristics described above, it is assumed that the size of each area is constant, but the thickness of each component in each area may be different. As shown in Fig. 14, the beams are divided into n segments. For an arbitrary section (i), the geometrical

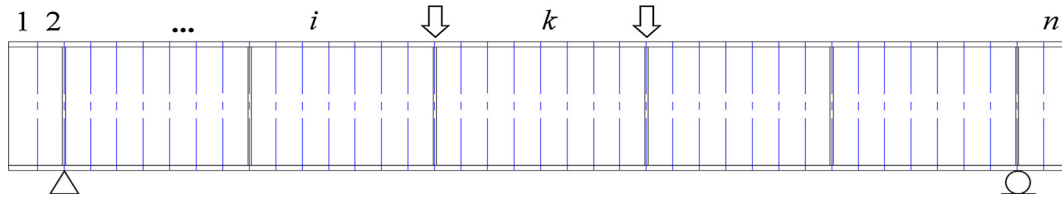


Fig. 14. Segment division.

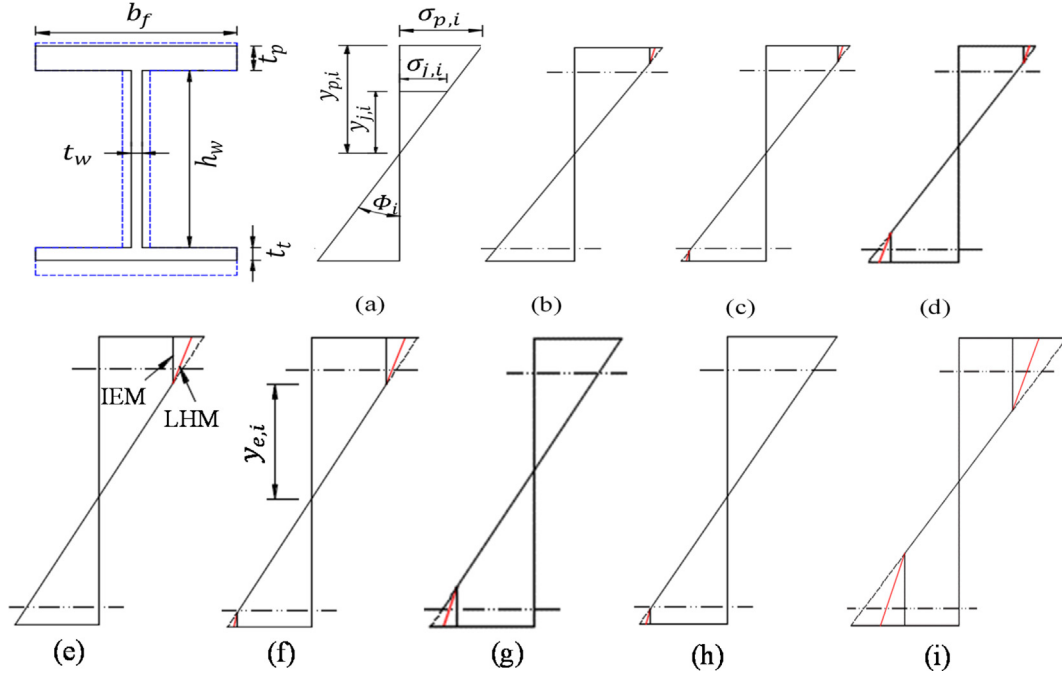


Fig. 15. Stress distribution.

parameters of the section, such as the sectional moment of inertia (I_i) and the static moment of area ($S_{p,i}$) [42], are constant. For a given load (P), the flexural moment (M_i) and shear (V_i) of the section can be easily determined. The effect of stiffeners on flexural resistance can be expressed as [40]

$$\varphi = 0.515 - 0.233 \times d/h_w + 0.041 \times (d/h_w)^2 \quad (12)$$

where φ = the influence coefficient of stiffener; and d = the distance between stiffeners.

Fig. 15 shows the stress distribution of the two models in all possible stress states resulting from non-uniform corrosion. For an arbitrary section i , the stress ($\sigma_{j,i}$) of arbitrary fiber j can be expressed as a function of the stress of the marginal elastic fibers on section i . Since the behavior of the tension region is similar to that of the compression region, models of the compression region are built as an example in this paper. The expression for $\sigma_{j,i}$ should be divided into two cases according to the height of the elastic region. The $\sigma_{j,i}$ of IEM and LHM can be expressed as Eq. (13) and Eq. (14), respectively.

$$\sigma_{j,i} = \begin{cases} \sigma_{e,i} y_{j,i} / y_{e,i}, & y_{j,i} \leq y_{e,i} \\ f_{ry}, & y_{e,i} < y_{j,i} < y_{p,i} \end{cases} \quad (13)$$

$$\sigma_{j,i} = \begin{cases} \sigma_{e,i} y_{j,i} / y_{e,i}, & y_{j,i} \leq y_{e,i} \\ E_s \varepsilon_{tr} (1 - w(\varepsilon_{tr})), & y_{e,i} < y_{j,i} < y_{p,i} \end{cases} \quad (14)$$

where $\sigma_{e,i}$ = the stress of marginal elastic fibers on section i ; $y_{j,i}$ = the distance from the neutral axis to fiber j ; $y_{e,i}$ = the distance from the neutral axis to the marginal elastic fibers i , and $y_{e,i} = y_{p,i}$ when the section is in full-section elastic state; and f_{ry} = the real yield stress of

flange or web.

For any section i , the equilibrium equations of force and flexural moment should be satisfied as follows:

$$\sum F_i = \int_{y_t}^{y_p} \sigma_{j,i} b(y) dy = 0 \quad (15)$$

$$\int_{y_t}^{y_p} \sigma_{j,i} b(y) y dy = M(i) \quad (16)$$

By simplification, the resistance moments of the section for IEM and LHM can be expressed as Eqs. (17) and (18), respectively.

$$M(i) = \begin{cases} I_{e,i} \sigma_{p,i} / y_{p,i}, & \text{elastic state} \\ f_{ry} (I_{e,i} / y_{e,i} + S_{pp,i}), & \text{elastic - plastic state} \end{cases} \quad (17)$$

$$M(i) = \begin{cases} I_{e,i} \sigma_{p,i} / y_{p,i}, & \text{elastic state} \\ f_{ry} (I_{e,i} / y_{e,i} + (1 - E_{sp} / E_s) S_{pp,i} + I_{p,i} E_{sp} / (E_s y_{e,i})) & , \text{elastic - plastic state} \end{cases} \quad (18)$$

where $I_{e,i}$ and $I_{p,i}$ = the sectional moment of inertia in the elastic region and in the elastic-plastic region, respectively; $S_{pp,i}$ = the static moment in the elastic-plastic region; and $\sigma_{p,i}$ = the stress of the top fibers on section i .

There are some differences in the flexural moment ($M(i)$) for the two models in the elastic-plastic stage. For IEM, it consists of elastic moment in elastic zone ($f_{ry} (I_{e,i} / y_{e,i})$) and plastic moment in plastic zone ($f_{ry} S_{pp,i}$). For LHM, it consists of elastic moment in elastic zone ($f_{ry} (I_{e,i} / y_{e,i})$), and elastic moment ($f_{ry} (1 - E_{sp} / E_s) S_{pp,i}$) and plastic moment in elastic-plastic zone ($f_{ry} I_{p,i} E_{sp} / (E_s y_{e,i})$). Thus, this expression can clearly show the composition of the flexural moments. Further, the

parameters ($I_{e,i}$), ($J_{p,i}$), and ($S_{pp,i}$) are the functions of the height of the elastic region $y_{s,i}$. Therefore, $y_{s,i}$ can be calculated and used to obtain the curvature of the section ($\Phi(i)$). The relation between the height of the elastic region ($y_{s,i}$) and the curvature ($\Phi(i)$) is expressed as follows:

$$\Phi(i) = \begin{cases} \sigma_{p,i}/E_s y_{s,i}, & \text{elastic state} \\ f_{ry}/E_s y_{s,i}, & \text{elastic - plastic state} \end{cases} \quad (19)$$

Due to the uneven section characteristics caused by corrosion, the position of the maximum deflection of the beams is uncertain, which makes it difficult to determine the deflection of segment i . The maximum deflection segment k can be determined using the principle that the deflection calculated from both sides is equal [41] and can be determined by

$$w(k)_{max,l} = \sum_1^k \Phi(k)x_{l,k} \times l_n$$

$$w(k)_{max,r} = \sum_1^k \Phi(k)x_{r,k} \times l_n$$

$$w(k)_{max,l} = w(k)_{max,r} = w(k)_{max} \quad (20)$$

where $w(k)_{max,l}$ and $w(k)_{max,r}$ = the deflection of segment k calculated from left and right, respectively; $w(k)_{max}$ = the maximum deflection; $x_{l,k}$ and $x_{r,k}$ = the distance between segment k to the support from left and right, respectively; and l_n = the length of the segment.

Therefore, the deflection of segment i can be calculated by

$$w(i) = w(k)_{max} - \sum_{p=i}^k \Phi(p)x_{p,i} \times l_n \quad (21)$$

where $w(i)$ is the deflection of segment i , and $x_{p,i}$ is the the distance from segment p to segment i .

The stress of each section of the whole beam is calculated to analyze the failure mechanism of the steel beam effected by corrosion. The flexural stress of fiber j at section i $\sigma_{j,i}$ and equivalent stress $\sigma_{eq,ji}$ based on distortion energy theory are calculated and analyzed [42]. The equivalent stress $\sigma_{eq,ji}$ is expressed as

$$\sigma_{eq,ji} = \sqrt{\sigma_{j,i}^2 + 3\tau_i^2}$$

$$\tau_i = V(i)S_{p,i}/I_t t_{w,i} \quad (22)$$

where τ_i = shear stress of section i , and is assumed constant across the section i .

4.2. Calculation procedure

As mentioned above, the failure behaviors of steel beams are various as the corrosion level changes. For a beam divided into n segments, it is recommended that the segments spacing (2 mm here) in the longitudinal direction be larger, and the spacing (0.1 mm here) in the cross-sectional direction be smaller in order to balance the calculation time and accuracy requirements. For a given load, flexural behaviors, such as the forces, moments, the height of the elastic region of segments, and the curvatures, can be determined. The flexural response of the whole process can be defined by increasing the load. Finally, the ultimate strength of the steel beam can be determined when the height of the elastic compression zone becomes zero. Fig. 16 shows the flowchart, and main calculation steps are listed as follows:

- Divide the beam into n segments;
- Input and calculate basic parameters for each segment;
- Suppose an initial load P and depth of compressive zone $y_{p,i}$, and calculate the flexural moment (M_i) and the shear (V_i);
- Revise the depth of compressive zone $y_{p,i}$ until the equilibrium equations of force and moment [Eqs. (15), (16)] are satisfied;

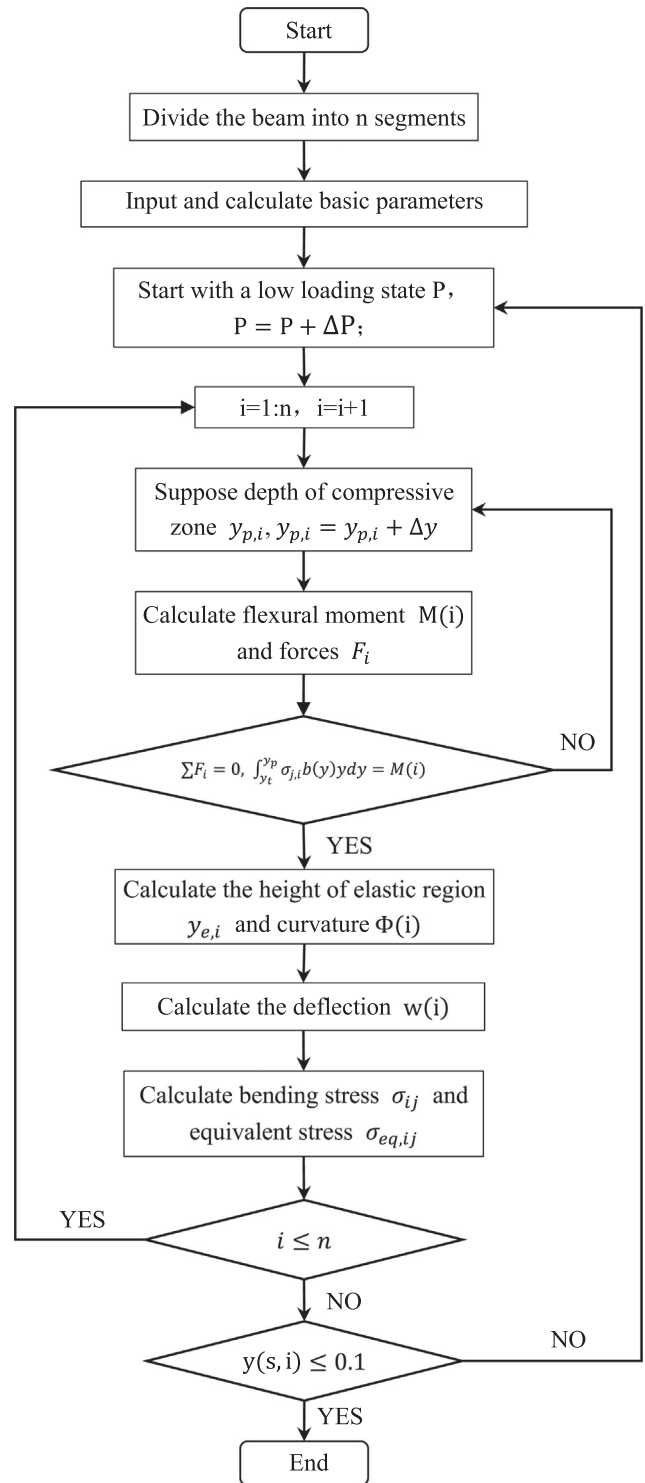


Fig. 16. Calculating flowchart of the procedure.

- Calculate the height of the elastic region $y_{s,i}$;
- Calculate the curvature of the segment ($\Phi(i)$) for all segments using the Eq. (19);
- Calculate the deflection of the segment $w(i)$ by the Eqs. (20) and (21);
- Calculate the flexural stress $\sigma_{j,i}$ and equivalent stress $\sigma_{eq,ji}$ using the Eqs. (13), (14) and (22), and;
- Increase the load until that the height of the elastic region (c) of the segment is close to 0.

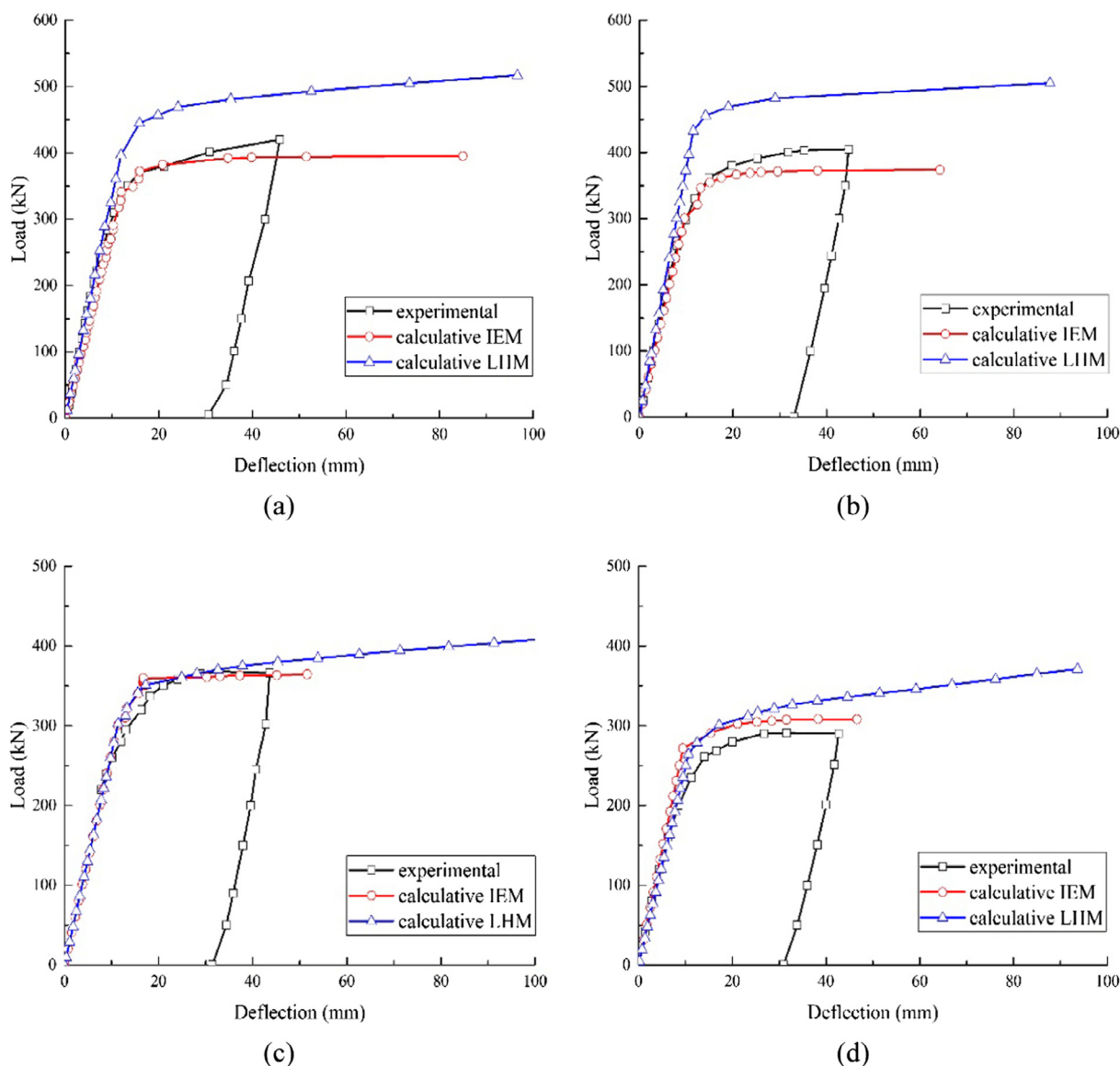


Fig. 17. Load-deflection curves: (a) CB0; (b) CB5; (c) CB10; and (d) CB15.

4.3. Discussion

The load-deflection curves at the maximum deformation are compared with the test results as shown in Fig. 17. The deformation curves almost coincide at the elastic state. After entering the elastic-plastic stage, the curves show obvious deviations. However, this phenomenon becomes less obvious as the degree of corrosion increases. This may be due to the ignorance of yield platform and approximation processing of the stress-strain constitutive relationship. This difference will be reduced gradually for serious specimens as corrosion shortens the yield platform. The predicted deflection of IEM is close to the experimental results, while the deflection curves of LHM is greater than those from the experimental results. With an increase of corrosion damage, the results of both IEM and LHM are in good agreement with the experimental results before the tested beams are failed. This is mainly attributed to the fact that the increasing corrosion damage gradually reduces the hardening modulus.

Figs. 18 and 19 show the flexural and equivalent stress cloud diagrams of the two models of CB0 and CB15 under the ultimate state. The stress at the buckling position of the test beam approaches the ultimate strength. The local buckling position of the tested beam is consistent with the maximum stress position. Thus the proposed model is well

matched with the experimental data. Compared with IEM, the range of the yield stress of LHM is wider, and the stress value before yield is higher. The shear area around the stiffeners yields first in the equivalent stress model, while the yielding stress in the flexural stress model appears first in the mid-span section. Affected by the corrosion inhomogeneity, the stress diagrams appear to be asymmetrical, and obvious folds and faults are shown in the figure. The distribution of the yield stress has been changed. And the boundary between the compressive stress and tensile stress, as shown in Fig. 19, is not a horizontal line in the longitudinal direction, which means the height of the neutral axis varies along the longitudinal direction of the beam.

The ultimate bearing capacity predicted by the standard of AISC, GB50017-2017, and the analytical model proposed in this paper are listed in Table 4. The ultimate moment of LHM is calculated at the moment of the same maximum deflection as the experimental results. The results calculated by the AISC are lower than the experimental values, while GB50017-2017 predicts higher results. The moment predicted by IEM shows good agreement with the test data, while the flexural strength calculated by LHM based on the real stress-strain relationship is higher than the experimental results. This may be affected by incomplete ideal test conditions and loading behavior. Namely, LHM provides a higher capacity and fits well with the GB50017-2017, and

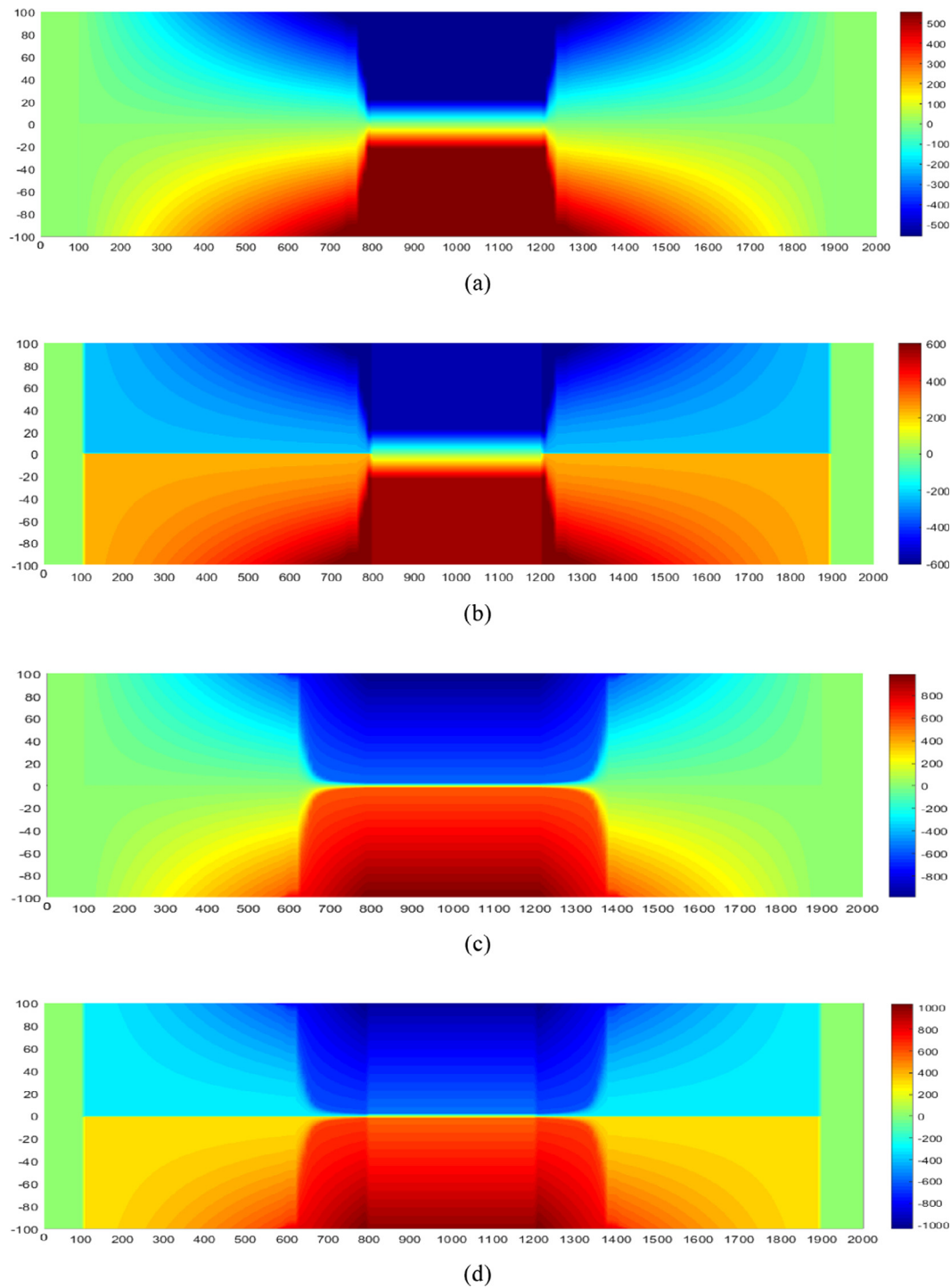


Fig. 18. Flexural and equivalent stress of IEM and LHM for CBO: (a) flexural stress of IEM; (b) equivalent stress of IEM; (c) flexural stress of LHM; and (d) equivalent stress of LHM.

IEM agrees well with the experimental results. Therefore, IEM and LHM or the GB50017-2017 can be regarded as the lower and upper limit values of the ultimate flexural moment respectively, and the results predicted by AISC are conservative.

5. Conclusions

The flexural behavior of corroded HPS beams is investigated in this paper. 3D scanning technology is employed to determine the geometric features of the tested beams. The impact of corrosion on strength and

deformation are discussed. An analytical model is proposed to predict the flexural strength of corroded HPS beams. Several conclusions are drawn based on this study:

- (1) As the corrosion level increases, the discreteness of the residual sectional area decreases and the compressed flange transforms from noncompact to slender.
- (2) Slight corrosion loss within 10% has little impact on both strength and stiffness degradation. Severe corrosion results in significant deterioration of the structural strength and stiffness.

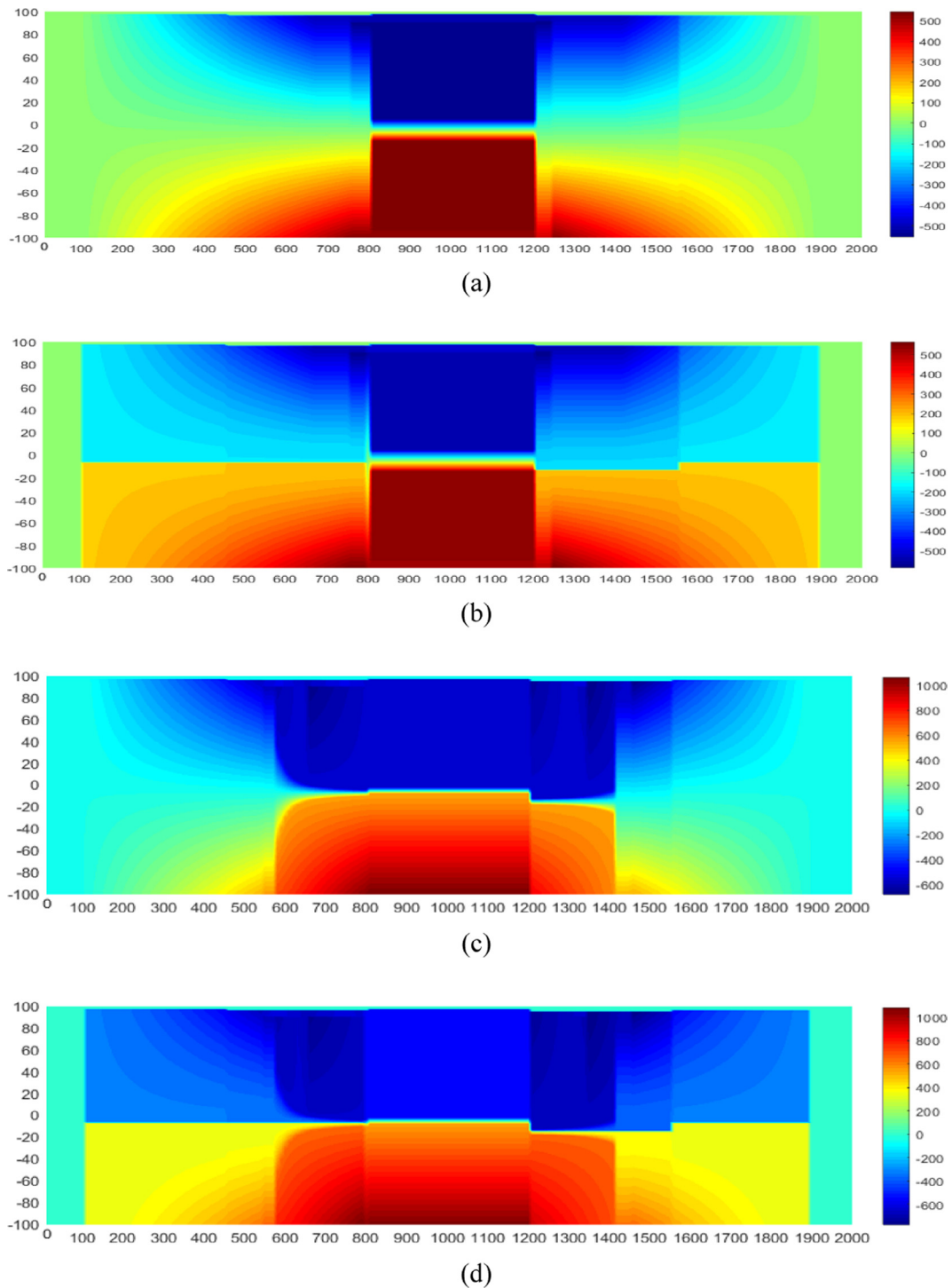


Fig. 19. Flexural and equivalent stress of IEM and LHM for CB15: (a) flexural stress of IEM; (b) Equivalent stress of IEM; (c) flexural stress of LHM; and (d) equivalent stress of LHM.

Table 4
Ultimate flexural moment.

No.	Experiment (M_e)	AISC		GB50017-2017		Proposed			
		M_A	M_A/M_e	M_G	M_G/M_e	LHM (M_L)	M_L/M_e	IEM (M_I)	M_I/M_e
CB0	148.75	114.22	0.77	168.54	1.13	173.25	1.16	138.25	0.93
CB5	142.45	110.01	0.77	145.04	1.02	161.35	1.13	130.86	0.92
CB10	128.8	94.05	0.73	130.32	1.01	133.00	1.03	127.50	0.99
CB15	101.85	83.48	0.82	118.99	1.17	122.85	1.21	107.84	1.06

- (3) The depth and length of the buckling wavelength for the corroded beams decrease gradually as the buckling resistance of the compressed flange decreases gradually when corrosion damage becomes serious and uneven, but it has little impact on strain development.
- (4) The proposed model IEM and LHM are verified by experimental results and compared with specifications. IEM and LHM or the GB50017-2017 may be suitable for predicting the lower and upper limit values of the ultimate flexural moment respectively, and the results predicted by AISC are conservative.

It should be noted that these findings are suitable for HPS beams subjected to electrochemical general corrosion. The current conclusions are based on a test of one beam for each corrosion level. Corrosion is a random and various process, and more tests, analysis and validation are required to generalize these findings. And more studies are required to analyze the impact of natural and random corrosion on flexural behavior as partial non-uniform corrosion is under consideration in this paper.

Declaration of Competing Interest

None.

Acknowledgements

The work reported here was conducted with financial support from the National Basic Research Program of China (No. 2015CB057701), the Guangdong Natural Science Foundation (No. 2015A030310141), and the Hunan Provincial Natural Science Foundation (No. 2018JJ2438). These supports are deeply acknowledged.

References

- [1] Miki C, Homma K, Tominaga T. High strength and high performance steels and their use in bridge structures. *J Constr Steel Res* 2002;58(1):3–20.
- [2] Shi G, Ban HY, Shi YJ. Engineering application and recent research progress on high strength steel structures. *Ind Constr* 2012;42(1):1–164. [in Chinese].
- [3] Shi G, Hu FX, Shi YJ. Recent research advances of high strength steel structures and codification of design specification in China. *Int J Steel Struct* 2014;14(4):873–87.
- [4] Kayser CR, Swanson JA, Linzell DG. Characterization of material properties of HPS-485W (70 W) TMCP for bridge girder applications. *J Bridge Eng* 2006;11(1):99–108.
- [5] Shi G, Wang M, Bai Y, Wang F, Shi YJ, Wang YQ. Experimental and modeling study of high-strength structural steel under cyclic loading. *Eng Struct* 2012;37:1–13.
- [6] Wang CS, Duan L, Wang JM, Zheng L. Bending behavior and ductility test of high performance steel beam based on hybrid design. *China J Highway Transport* 2012;25(2):81–9. [in Chinese].
- [7] Li GQ. Experimental study on the ultimate bearing capacity of welded box-section columns using Q460 high strength steel in bending and axial compression. *China Civ Eng J* 2012;45(8):67–73. [in Chinese].
- [8] Li GQ, Wang YB, Chen SW, Cui W, Sun FF. Experimental study of Q460C high strength steel welded H-section and box-section columns under cyclic loading. *J Build Struct* 2013;34(3):80–6. [in Chinese].
- [9] Felkel JP, Rizos DC, Ziehl PH. Structural performance and design evaluation of HPS 70W bridge girders. *J Constr Steel Res* 2007;63(7):909–21.
- [10] Barth KE, Yang L, Righman J. Simplified moment redistribution of hybrid HPS 485W bridge girders in negative bending. *J Bridge Eng* 2007;12(4):456–66.
- [11] Yang YM, Peng JX, Zhang JR, Cai CS. A new method for estimating the scale of fluctuation in reliability assessment of reinforced concrete structures considering spatial variability. *Adv Struct Eng* 2018;21(13):1951–62.
- [12] Ma YF, Guo ZZ, Wang L, Zhang JR. Experimental investigation of corrosion effect on bond behavior between reinforcing bar and concrete. *Constr Build Mater* 2017;152:240–9.
- [13] Yamaguchi E, Akagi T, Tsuji H. Influence of corrosion on load-carrying capacities of steel I-section main-girder end and steel end cross-girder. *Int J Steel Struct* 2014;14(4):831–41.
- [14] Kim IT, Lee MJ, Ahn JH, Kainuma S. Experimental evaluation of shear buckling behaviors and strength of locally corroded web. *J Constr Steel Res* 2013;83:75–89.
- [15] Sharifi Y. Uniform corrosion wastage effects on the load-carrying capacity of damaged steel beams. *Adv Steel Constr* 2012;8(2):153–67.
- [16] Tohidi S, Sharifi Y. Load-carrying capacity of locally corroded steel plate girder ends using artificial neural network. *Thin-Walled Struct* 2016;100:48–61.
- [17] Khurram N, Sasaki E, Kihira H, Katsuchi H, Yamada H. Analytical demonstrations to assess residual bearing capacities of steel plate girder ends with stiffeners damaged by corrosion. *Struct Infrastruct Eng* 2014;10(1):69–79.
- [18] Sharifi Y, Rahgozar R. Remaining moment capacity of corroded steel beams. *Int J Steel Struct* 2010;10(2):165–76.
- [19] Sharifi Y, Rahgozar R. Fatigue notch factor in steel bridges due to corrosion. *Arch Civ Mech Eng* 2009;9(4):75–83.
- [20] Wu W, Hao WK, Liu ZY, Li XG, Du CW, Liao WJ. Corrosion behavior of E690 high-strength steel in alternating wet-dry marine environment with different pH values. *J Mater Eng Perform* 2015;24(12):4636–46.
- [21] Ma HC, Liu ZY, Du CW, Wang HR, Li CY, Li XG. Effect of cathodic potentials on the SCC behavior of E690 steel in simulated seawater. *Mater Sci Eng A* 2015;642:22–31.
- [22] López A, Bayón R, Pagano F, Igartua A, Arredondo A, Arana JL, et al. Tribocorrosion behaviour of mooring high strength low alloy steels in synthetic seawater. *Wear* 2015;338–339:1–10.
- [23] Akiyama E, Wang M, Li S, Zhang Z, Kimura Y, Uno N, et al. Studies of evaluation of hydrogen embrittlement property of high-strength steels with consideration of the effect of atmospheric corrosion. *Metall Mater Trans A* 2013;44(3):1290–300.
- [24] GB. Code for design of steel structure. *GB5017-2017*; 2017.
- [25] Kashani MM, Crewe AJ, Alexander NA. Use of a 3D optical measurement technique for stochastic corrosion pattern analysis of reinforcing bars subjected to accelerated corrosion. *Corrosion Sci* 2013;73:208–21.
- [26] Fernandez I, Bairán JM, Marí AR. 3D FEM model development from 3D optical measurement technique applied to corroded steel bars. *Constr Build Mater* 2016;124:519–32.
- [27] Wang XG, Zhang WP, Gu XL, Dai HC. Determination of residual cross-sectional areas of corroded bars in reinforced concrete structures using easy-to-measure variables. *Constr Build Mater* 2013;38:846–53.
- [28] Mancini G, Tondolo F, Iuliano L, Minetola P. Local reinforcing bar damage in r.c. members due to accelerated corrosion and loading. *Constr Build Mater* 2014;69:116–23.
- [29] Tang FJ, Lin ZB, Chen GD, Yi WJ. Three-dimensional corrosion pit measurement and statistical mechanical degradation analysis of deformed steel bars subjected to accelerated corrosion. *Constr Build Mater* 2014;70:104–17.
- [30] AISC. Specification for structural steel buildings. *ANSI/AISC 360-10*; 2010.
- [31] Maaddawy TAE, Soudki KA. Effectiveness of impressed current technique to simulate corrosion of steel reinforcement in concrete. *J Mater Civ Eng* 2003;15(1):41–7.
- [32] Xiao LF, Peng JX, Zhang JR, Cai CS. Mechanical properties of corroded high performance steel specimens based on 3D scanning. *Adv Steel Constr* 2019;15(2). <https://doi.org/10.18057/IJASC.2018.14.2.2>.
- [33] Earls CJ. On the inelastic failure of high strength steel I-shaped beams. *J Constr Steel Res* 1999;49(1):1–24.
- [34] Shokouhian M, Shi Y. Classification of I-section flexural members based on member ductility. *J Constr Steel Res* 2014;95:198–210.
- [35] AASHTO, AASHTO LRFD bridge design specifications; 2007.
- [36] Younes RM, Abu-Farsakh GA, Hunaiti YM. Effect of welding on lateral-torsional buckling resistance of I-shaped built-up steel. *Jordan J Civ Eng* 2009;3(4):295–313.
- [37] Nakai T, Matsushita H, Yamamoto N. Effect of pitting corrosion on local strength of hold frames of bulk carriers (2nd Report)—Lateral-distortional buckling and local face buckling. *Mar Struct* 2004;17(8):612–41.
- [38] Yang B, Xiong G, Ding K, Nie S, Zhang W, Hu Y, et al. Experimental and numerical studies on lateral-torsional buckling of GJ structural steel beams under a concentrated loading condition. *Int J Struct Stab Dyn* 2016;16(01):1640004.
- [39] Zhang WP, Dai HC, Gu XL, Wu SN. Effects of corrosion pits on mechanical properties of corroded steel bars. *Earth and space 2010: Engineering, Science, Construction, and Operations in Challenging Environments*, Reston, Reston; 2010.
- [40] Liu WB. Experimental study on bearing capacity of partially rusted H-type high performance steel beam and numerical simulation. *Changsha: Changsha University of Science & Technology*; 2018.
- [41] Maaddawy TE, Soudki K, Topper T. Analytical model to predict nonlinear flexural behavior of corroded reinforced concrete beams. *ACI Struct J* 2005;102(4):550–9.
- [42] Sun XF, Fang SX, Guan TL. *Mechanics of materials (I)*. 5th ed. Higher Education Press; 2013.